KFUPM
Journal of Undergraduate Research International

Diamond Open Access 76

Article Control and Instrumentation Engineering

A New Variable-Exponent Predefined-Time Sliding Mode Control for the Energy Management of Battery-Fuel Cell Hybrid Electric Vehicles

Maryam Abdulaziz Alsalman and Syed Muhammad Amrr*

Cite https://doi.org/10.64589/juri/231588

Submitted: April 25, 2026 **Revised:** May 09, 2026 **Accepted:** May 11, 2026

ABSTRACT

Despite recent improvements to battery-powered electric vehicles, they face limitations related to limited driving range, long charging times, and accelerated battery degradation under demanding duty cycles. In addition, existing methods for addressing these issues may be impractical in real-world applications. This study addresses this gap by investigating a robust energy management approach for a fuel cell electric vehicle (FCEV) with hybrid power sources. In this system, the fuel cell serves as the main power source, whereas a lithium-ion battery and an ultracapacitor provide additional support to handle load variations and transient conditions. The fuel cell is connected to the DC link through a DC–DC boost converter, whereas the battery and ultracapacitor are interfaced via bidirectional converters to allow flexible power exchange. A fourth-order dynamic model that accounts for model uncertainties and voltage fluctuations is developed to accurately represent system behavior. In addition, a new variable-exponent-based predefined-time sliding mode control strategy is introduced. This controller is designed to coordinate power sharing among multiple sources and effectively regulate the DC-link voltage across different operating conditions. Simulation results are presented to verify the effectiveness of the proposed control scheme. The results demonstrate that the system achieves fast response, stable voltage regulation, and reliable energy distribution. The proposed method guarantees predefined-time stability, i.e., the system states reach their desired values within a predefined time regardless of initial conditions. In addition, the controller improves robustness against uncertainties and reduces the effect of disturbances, making it suitable for practical FCEV applications.

Keywords: hybrid energy management, DC–DC power converters, electric vehicles, robustness, predefined-time stability

The following symbols and parameters are used throughout the manuscript.

Symbol	Description
i_{fc}, v_{fc}	Fuel cell current and voltage (converter input)
i_b, v_b	Battery current and voltage (converter input)
i_{uc}, v_{uc}	Ultracapacitor (UC) current and voltage (converter input)
v_{dc}	DC-link (DC bus) voltage
i_o	Load (motor drive) current drawn from the DC bus
$i_{fc,r}$, $i_{b,r}$, $i_{uc,r}$	Reference currents for the fuel cell, battery, and UC
$v_{dc,r}$	Reference DC-link voltage
δ_{fc}	Boost-converter duty ratio
δ_b	Duty ratio of the battery bidirectional converter
δ_{uc}	Duty ratio of the UC bidirectional converter
$\delta_b^{(1)}$, $d_b^{(2)}$	Battery switch duty ratios for charge/discharge modes
$\delta_{uc}^{(1)}$, $d_{uc}^{(2)}$	UC switch duty ratios for charge/discharge modes
L_{fc}, R_{fc}	Fuel cell converter inductor and series resistance
L_b, R_b	Battery converter inductor and series resistance
L_{uc}, R_{uc}	UC converter inductor and series resistance
C_{dc}	DC-link capacitance
Δv_{fc}, Δv_b, Δv_{uc}	Voltage fluctuation in respective sources
$\mathbf{\Delta}$	Uncertainty vector
K	Mode indicator ($K = 1$ discharge, $K = 0$ charge)
σ	Boost-converter ideality factor
ε_1, ε_2, ε_3	Tracking errors for i_{fc}, i_b, i_{uc}
$\mathbf{\Sigma}$	Integral sliding variable
$\|\cdot\|$	Two-norm
$\mathcal{K}_1$, $\mathcal{K}_2$	Predefined-time controller gains

Published under an exclusive license by KFUPM

c_1	Switching gain
$\ell_1, \ell_2, \upsilon_0$	Sliding surface and control coefficients
$\lambda_1, \lambda_2, \beta_1, \beta_2$	Various exponents
Δ	Upper bound of uncertainties

1. INTRODUCTION

Reducing greenhouse gas emissions and limiting dependence on fossil fuels have made transportation electrification an active area of research [1–3]. Although battery-powered electric vehicles have improved considerably in recent years, they still face well-known limitations, such as limited driving range, long charging times, and accelerated battery degradation under demanding duty cycles [4,5]. These drawbacks have motivated the development of hybrid architectures combining complementary energy sources. Among them, fuel cell electric vehicles (FCEVs) are particularly promising: proton exchange membrane fuel cells (PEMFCs) can serve as the primary power source for an extended range, and auxiliary devices such as lithium-ion batteries and ultracapacitors (UCs) compensate for the limited transient capability of the fuel cell [6]. PEMFCs are attractive for sustainable transportation because they offer high electrical efficiency (up to approximately 50%) and produce zero tailpipe emissions [7,8]. However, the electrochemical processes inside a PEMFC, including membrane hydration and reactant gas transport, impose inherent response delays that prevent the fuel cell from following rapid power demands on its own [9]. During events such as hard acceleration or regenerative braking, these delays can cause a mismatch between the power requested by the drivetrain and the power delivered by the fuel cell. Consequently, an FCEV typically requires supplementary energy storage that can absorb or release power on a faster time scale. Figure 1 shows the diagram of a hybrid power system (HPS) in an FCEV with multiple energy sources.

To address this issue, various approaches are used. The first category among these is that many FCEVs use an HPS that includes multiple sources and power electronic converters. As illustrated in Figure 1, the HPS is responsible for energy buffering, coordinated power sharing, and supplying the motor drive [9–11]. Within this architecture, three sources play complementary roles. The battery offers high energy density (typically 250–350 Wh/kg for lithium-ion batteries) and is well suited for sustained power delivery over moderate time scales [12]. By contrast, the UC has a lower energy density but can deliver or absorb high-power pulses almost instantaneously, making it ideal for short transients. Therefore, combining these three sources improves vehicle performance across a wide range of driving conditions. Concurrently, differences in voltage levels and dynamic characteristics among sources introduce significant control challenges, particularly in maintaining a stable DC-bus voltage during rapid load changes [13].

Regulating the DC-bus voltage is a central control objective in any HPS because sudden load changes from the motor drive or source output fluctuations can degrade system reliability. Various control strategies have been investigated to address this problem, and they can be broadly grouped into two categories. The first category includes data-driven and intelligent methods. Neural network and fuzzy logic controllers have been proposed to improve power sharing and voltage regulation under varying operating conditions [14,15]. Model predictive control (MPC) has also been applied to battery–supercapacitor subsystems to manage transient loads while keeping the bus voltage within acceptable limits [4]. More recently, hybrid intelligent schemes such as fuzzy-MPC integration have been reported to reduce steady-state error and improve transient response [16]. Although these methods can handle nonlinear system behavior, they typically require accurate training data or detailed prediction models, and their computational cost may limit real-time applicability in resource-constrained vehicle platforms.

The second category comprises model-based robust control approaches. Backstepping designs combined with sliding mode control (SMC) have been used for fuel cell–supercapacitor systems to handle nonlinearities and parameter uncertainties [17]. Adaptive and terminal SMC schemes have been developed for multi-source HPSs to enforce finite-time convergence of tracking

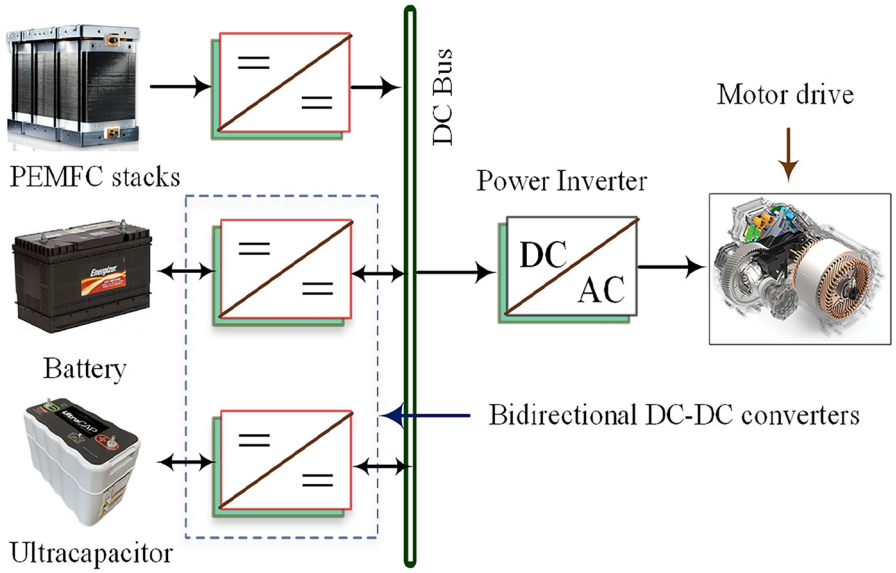

Figure 1. Block diagram for the HPS in an FCEV

errors [18–21]. Bilinear modeling together with Lyapunov-based controllers has also been explored to improve stability guarantees and capture the inherently nonlinear converter dynamics [22–24]. Backstepping–super-twisting control has further been proposed to attenuate chattering while maintaining robustness [25]. Despite these advances, most existing methods focus on high-level energy management and do not explicitly address converter-level stabilization of the DC-bus voltage under simultaneous source-side uncertainties and load-side disturbances. Moreover, conventional SMC schemes employ fixed gains that often produce excessive chattering near the equilibrium, degrading power quality and increasing converter stress.

To address these limitations, a variable-exponent (VE) SMC approach has recently been developed, in which the exponents of the sliding surface and the controller adapt to time-varying state variables [26–29]. Conceptually, this design facilitates aggressive error reduction when deviations are large and transitions to a smoother control action as errors approach zero. Thus, it effectively mitigates chattering without compromising convergence speed. Although these VE designs ensure fixed-time (FxT) stability, achieving a specific settling time often requires the tedious tuning of multiple parameters, which can be impractical for real-time applications. More recently, a predefined-time (PdT) variable-exponent control was proposed [30], allowing the settling time to be directly specified via an explicit parameter. Inspired by this framework, this study develops a robust VE-PdT-SMC for FCEV systems, ensuring effective DC-link voltage regulation during high transients, such as acceleration and regenerative braking.

From the aforementioned literature review, two practical limitations remain unresolved. First, existing VE-SMC designs achieve fixed-time stability but require simultaneous tuning of multiple exponents and gains to enforce a specific settling time, which is impractical for safety-critical automotive controllers where the settling time must be guaranteed by design. Second, the recent VE predefined-time formulation [30] was developed for input-constrained spacecraft attitude regulation and has not been extended to the multi-source converter dynamics encountered in FCEV power management. Consequently, control strategies that can simultaneously address (i) predefined-time DC-link regulation independent of initial conditions, (ii) robustness against both source-side voltage uncertainties and load-side disturbances arising from realistic driving cycles, and (iii) chattering reduction using a VE structure designed for triple-source FCEV hybrid powertrains are necessary. A concise comparison of representative control strategies for FCEV/HPS power management against the proposed VE-PdT-SMC is provided in Table 1.

The main contributions of this work are summarized as follows:

- A novel VE-PdT-SMC scheme is developed at the converter level to achieve robust DC-bus voltage stabilization in a triple-source FCEV HPS, guaranteeing predefined-time convergence of the regulation error. Compared with VE fixed-time designs [27–29], the proposed scheme enforces the settling time through a single explicit parameter (T_d), eliminating the iterative tuning of multiple exponents required by previous formulations and yielding a settling-time bound that is independent of the initial states.
- The proposed control structure is analyzed under simultaneous load-side disturbances and source-side uncertainties, including representative acceleration and regenerative braking scenarios.
- The stability of the proposed controller is rigorously established using Lyapunov analysis, ensuring that the system states converge to their desired values within a predefined-time bound regardless of initial conditions.
- The effectiveness of the proposed method is validated through matrix laboratory (MATLAB) simulations, demonstrating fast response, stable voltage regulation, and reliable energy distribution under different operating conditions.

The remainder of this paper is organized as follows: Section 2 describes the HPS dynamic modeling and control objective. Mathematical preliminaries for predefined-time stability and construction of the proposed VE-PdT-SMC are presented in Section 3. A detailed theoretical stability verification is established in Section 4. The effectiveness of the proposed strategy is demonstrated through simulation results in Section 5. Finally, the conclusions are summarized in Section 6.

2. DYNAMIC MODELING OF THE HPS

In FCEVs, the HPS relies on coordinated control and energy management strategies, integrating fuel cells, batteries, and UCs to meet the demand of the motor drive. The typical HPS architecture is illustrated in Figure 2, and its detailed mathematical modeling and subsystem dynamics are elaborated in the following section. For clarity, all nomenclature and parameter definitions used throughout this work are summarized in the Nomenclature section preceding the Introduction section.

Table 1. *Comparison of representative control strategies for FCEV/HPS power management*

Control strategy	Convergence	Robustness	Chattering	Tuning effort	FCEV converter-level DC-link regulation
Fuzzy / NN [14,15]	Asymptotic	Data-dependent	Low	High (training)	Limited
MPC / Fuzzy-MPC [4,16]	Finite horizon	Model-dependent	None	Medium	Partial
Backstepping-SMC [17]	Asymptotic	High	High	Medium	Limited
Adaptive / Terminal SMC [19–21]	Finite time	High	Reduced	MediumHigh	Partial
VE-FxT-SMC [27–29]	Fixed time	High	Low	High (multi-exponent)	Not addressed
Proposed VE-PdT-SMC	**Predefined time**	**High**	**Low**	**Reduced (explicit)**	**Yes (triple-source)**

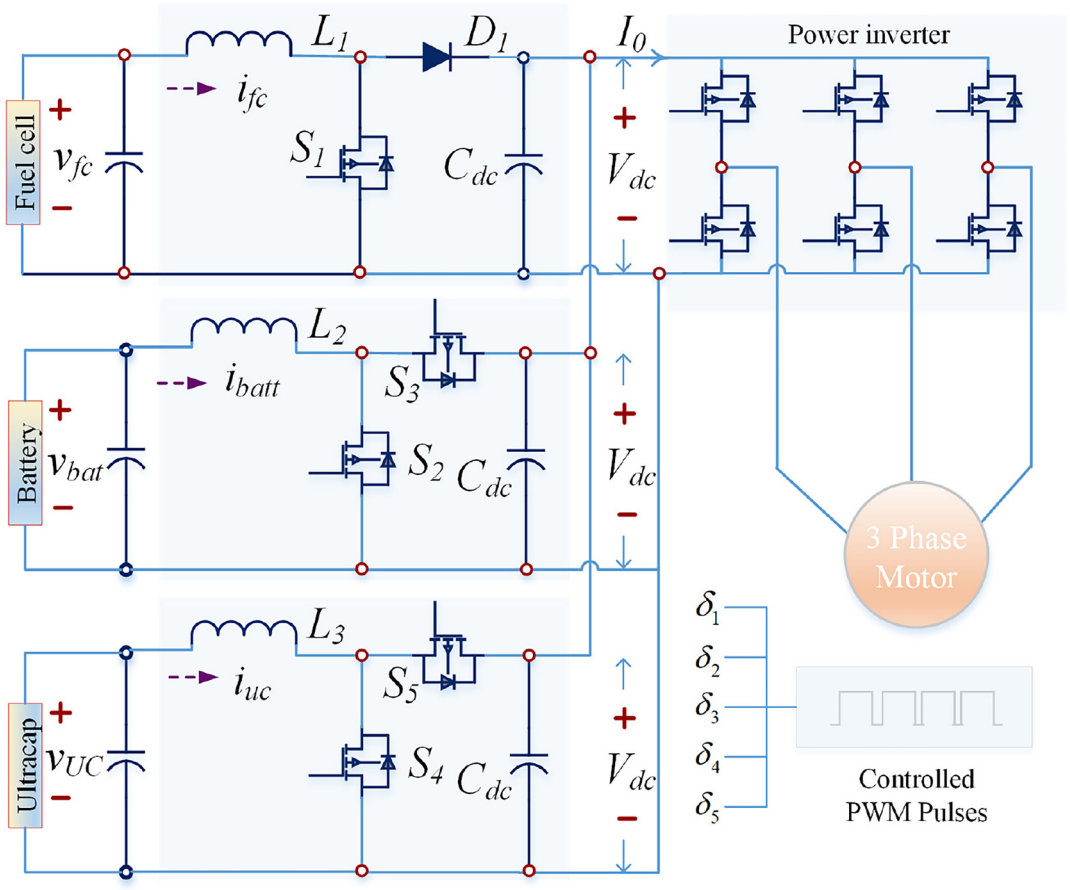

Figure 2. Circuit configuration of the HPS in an FCEV

2.1. Modeling of DC–DC Converters. The fuel cell is interfaced with the powertrain through a unidirectional boost converter comprising a switch, a diode, an inductor, and a capacitor. The operation of the fuel cell is controlled via pulse width modulation (PWM) with duty ratio (δ_{fc}), and the average dynamic model is expressed by Equations (1) and (2)[31]:

$$\frac{di_{fc}}{dt} = -(1-\delta_{fc})\frac{v_{dc}}{L_{fc}} - \frac{R_{fc}}{L_{fc}}i_{fc} + \frac{v_{fc}}{L_{fc}}, \tag{1}$$

$$\frac{dv_{dc}}{dt} = (1-\delta_{fc})\frac{i_{fc}}{C_{dc}} - \frac{1}{C_{dc}}\frac{di_{fc}}{dt}, \tag{2}$$

where i'' and v_{fc} denote the fuel cell current and voltage at the converter input, respectively, and v_{dc} denotes the DC-link voltage.

2.2. Bidirectional Converter. The battery and UC are connected to the DC bus through bidirectional buck–boost converters, each comprising an inductor, a capacitor, and two high-frequency switches[32]. The switches are controlled via PWM duty ratios $\delta_b^{(1)}$, $\delta_b^{(2)}$ for the battery and $\delta_{uc}^{(1)}$, $\delta_{uc}^{(2)}$ for the UC, depending on whether the converters are operating in charging or discharging mode. The battery dynamics are given by Equations (3) and (4):

$$\left.\frac{di_b}{dt}\right| = -\delta_b\frac{v_{dc}}{L_b} - \frac{R_b}{L_b}i_b + \frac{v_b}{L_b}, \tag{3}$$

$$\text{where } \delta_b| = K\left(1-\delta_b^{(1)}\right) + (1-K)\,\delta_b^{(2)}, \tag{4}$$

where K is mode-dependent, taking $K = 1$ during discharging, and $K = 0$ otherwise. A similar dynamic model is used for the UC framework, which is expressed by Equations (5) and (6):

$$\frac{di_{uc}}{dt} = -\delta_{uc}\frac{v_{dc}}{L_{uc}} - \frac{R_{uc}}{L_{uc}}i_{uc} + \frac{v_{uc}}{L_{uc}} \tag{5}$$

where

$$\delta_{uc} = K\left(1-\delta_{uc}^{(1)}\right) + (1-K)\,\delta_{uc}^{(2)} \tag{6}$$

2.3. Overall HPS Modeling. The complete dynamic model of the HPS is governed by Equation (7a–d). These expressions capture the essential behavior of the hybrid sources required to effectively design and evaluate the FCEV powertrain:

$$\frac{di_{fc}}{dt} = -\frac{R_{fc}}{L_{fc}} i_{fc} + \frac{1}{L_{fc}} (v_{fc} + \Delta v_{fc}) - \frac{1 - \delta_{fc}}{L_{fc}} v_{dc} \quad (7a)$$

$$\frac{di_{b}}{dt} = -\frac{R_{b}}{L_{b}} i_{b} + \frac{1}{L_{b}} (v_{b} + \Delta v_{b}) - \frac{\delta_{b}}{L_{b}} v_{dc} \quad (7b)$$

$$\frac{di_{uc}}{dt} = -\frac{R_{uc}}{L_{uc}} i_{uc} + \frac{1}{L_{uc}} (v_{uc} + \Delta v_{uc}) - \frac{\delta_{uc}}{L_{uc}} v_{dc} \quad (7c)$$

$$\frac{dv_{dc}}{dt} = \frac{1 - \delta_{fc}}{C_{dc}} i_{fc} + \frac{\delta_{b}}{C_{dc}} i_{b} + \frac{\delta_{uc}}{C_{dc}} i_{uc} - \frac{1}{C_{dc}} i_{o} \quad (7d)$$

Let $i_{fc,r}$, $i_{b,r}$, $i_{uc,r}$, and $v_{dc,r}$ represent the reference fuel cell current, battery current, UC current, and DC-link voltage, respectively. The relation between $i_{fc,r}$ and $v_{dc,r}$ is expressed by Equation (8):

$$i_{fc,r} = \sigma \left(\frac{v_{dc,r} i_{o} - v_{uc} i_{uc} - v_{b} i_{b}}{v_{fc}} \right). \quad (8)$$

Here, σ is the ideality factor of the boost converter, and Equation (8) shows that $i_{fc} = i_{fc,r}$ implies $v_{dc} \to v_{dc,r}$.

2.4. Error Dynamic. The tracking errors associated with the fuel cell current (ε_1), battery current (ε_2), and UC current (ε_3) are expressed by Equation (9):

$$\varepsilon_1 = i_{fc} - i_{fc,r}, \varepsilon_2 = i_{b} - i_{b,r}, \varepsilon_3 = i_{uc} - i_{uc,r}. \quad (9)$$

The derivatives of the error variables in Equation (9) can be derived from the system dynamics in Equation (7) as expressed by Equation (10a–c):

$$\dot{\varepsilon}_1 = -\frac{R_{fc}}{L_{fc}} i_{fc} + \frac{1}{L_{fc}} (v_{fc} + \Delta v_{fc}) - \frac{\bar{\delta}_{fc}}{L_{fc}} v_{dc} - i_{fc,r}, \quad (10a)$$

$$\dot{\varepsilon}_2 = -\frac{R_{b}}{L_{b}} i_{b} + \frac{1}{L_{b}} (v_{b} + \Delta v_{b}) - \frac{\bar{\delta}_{b}}{L_{b}} v_{dc} - i_{b,r}, \quad (10b)$$

$$\dot{\varepsilon}_3 = -\frac{R_{uc}}{L_{uc}} i_{uc} + \frac{1}{L_{uc}} (v_{uc} + \Delta v_{uc}) - \frac{\bar{\delta}_{uc}}{L_{uc}} v_{dc} - i_{uc,r}, \quad (10c)$$

where $\delta_{fc} := 1 - \delta_{fc}$. Subsequently, Equation (10) can be rewritten in matrix form as Equation (11):

$$\dot{\boldsymbol{\varepsilon}} = \mathbf{A}\mathbf{i} - \mathbf{B}\mathbf{U} + \boldsymbol{\phi} + \boldsymbol{\Delta} - \mathbf{I}_{ref}, \quad (11)$$

where $\boldsymbol{\varepsilon} = [\varepsilon_1 \ \varepsilon_2 \ \varepsilon_3]^T$, $\mathbf{i} = [i_{fc} i_b i_{uc}]^T$, $\mathbf{U} = [\delta_{fc} \delta_b \delta_{uc}]^T$, and $\mathbf{i}_{ref} = [i_{fc,r} i_{b,r} i_{uc,r}]^T$. Moreover, $\phi = [v_{fc}/L_{fc} v_b/L_b | v_{uc}/L_{uc}]^T$, $\boldsymbol{\Delta} = [\Delta v_{fc}/L_{fc} \Delta v_b/L_b \Delta v_{uc}/L_{uc}]^T$, and

$$\mathbf{A} = \begin{bmatrix} -\frac{R_{fc}}{L_{fc}} & 0 & 0 \\ 0 & -\frac{R_{b}}{L_{b}} & 0 \\ 0 & 0 & -\frac{R_{uc}}{L_{uc}} \end{bmatrix}, \quad \mathbf{B} = \begin{bmatrix} \frac{v_{dc}}{L_{fc}} & 0 & 0 \\ 0 & \frac{v_{dc}}{L_{b}} & 0 \\ 0 & 0 & \frac{v_{dc}}{L_{uc}} \end{bmatrix}. \quad (12)$$

Assumption 1. All states (i_{fc}, i_b, i_{uc}, andv_{dc})are measurable, and the DC-bus voltage $v_{dc}$is positive.

Assumption 2. The system uncertainties $\boldsymbol{\Delta}$ are considered to be bounded as $\| \boldsymbol{\Delta} \| \leq \Delta$, with $\Delta > 0$.

2.5. Problem Statement. A robust control law is proposed to manage power sharing among the three sources and maintain the DC-bus voltage despite parametric uncertainties by adjusting the duty ratios of the HPS converters. The objective can be stated as: $\lim_{t \to t_{pd}} \varepsilon_1 (t) \approx 0$, $\lim_{t \to t_{pd}} \varepsilon_2 (t) \approx 0$, $\lim_{t \to t_{pd}} \varepsilon_3 (t) \approx 0$, $\lim_{t \to t_{pd}} \varepsilon_4 (t) \approx 0$, where t_{pd} denotes the prescribed settling time.

3. PRELIMINARIES AND PROPOSED CONTROLLER

This study presents a new VE-PdT-SMC design to achieve faster convergence and ensure robustness against system uncertainties and load fluctuations. To facilitate the design of the proposed controller, we first present a set of preliminary lemmas. These results establish the stability criteria necessary to guarantee the predefined-time convergence properties investigated in this study. The overall design philosophy is to first define an integral sliding surface whose dynamics already possess predefined-time convergence to zero (Lemma 3) and then to construct the control input so that the sliding variable is driven to zero in another predefined time. The two predefined-time bounds are independent of the initial conditions, and their sum yields a transparent worst-case settling time for the closed-loop tracking error.

3.1. Preliminaries. Consider a continuous-time system expressed by Equation (13):

$$\dot{z}(t) = g(z(t), u) \in \mathbb{R}^n \text{ with } z(0) = z_0 \quad (13)$$

where $z \in \mathbb{R}^n$ is the system state, $u \in \mathbb{R}^m$ is the control input, and $g(\cdot) : \mathbb{R}^n \times \mathbb{R}^m \to \mathbb{R}^n$ is a smooth vector field.

Lemma 1. Consider the system in Equation (13). Suppose a radially unbounded Lyapunov function $W(z)$exists satisfying the differential inequality expressed by Equation (14)[33]:

$$\dot{W} \leq -\mu_1 W^{\beta_1} - \mu_2 W^{\beta_2} + \delta, \quad (14)$$

where $\mu_1 > 0, \mu_2 > 0, 0 < \beta_1 < 1 < \beta_2$, and $\delta > 0$ is a positive constant. Under these conditions, the system is practically fixed-time stable, and the settling time satisfies Equation (15):

$$T_s (z_0) = \frac{\varrho}{\mu_1 (1 - \beta_1)} + \frac{\varrho}{\mu_2 (\beta_2 - 1)}, \quad (15)$$

where $0 < \varrho < 1$. Furthermore, the system trajectories converge to the residual set expressed by Equation (16):

$$\Omega = \left\{ x \mid W \leq \min \left\{ \left(\frac{\delta}{\mu_1 (1 - \varrho)} \right)^{\frac{1}{\beta_1}}, \left(\frac{\delta}{\mu_2 (1 - \varrho)} \right)^{\frac{1}{\beta_2}} \right\} \right\}. \quad (16)$$

Moreover, when $\delta = 0$,the inequality in Equation (14) reduces to Equation (17):

$$\dot{W} \leq -\mu_1 W^{\beta_1} - \mu_2 W^{\beta_2}, \quad (17)$$

and the system trajectories converge to the origin for all $t > T_s (z_0)$,where the settling time is expressed by Equation (18):

$$T_s (z_0) = \frac{1}{\mu_1 (1 - \beta_1)} + \frac{1}{\mu_2 (\beta_2 - 1)}. \quad (18)$$

Lemma 2. Following Lemma 1, suppose a radially unbounded Lyapunov function Wsatisfies Equation (17). If the parameters are selected as expressed by Equation (19):

$$\mu_1 = \frac{1}{T_d \cdot \lambda\,(1-\beta_1)}, \quad \mu_2 = \frac{1}{T_d\,(1-\lambda)\,(\beta_2-1)}, \tag{19}$$

where $0 < \lambda < 1$, and $T_d > 0$is the predefined settling time, then the system exhibits predefined-time stability. In particular, for all $t \geq T_d$,the state $z$converges to the origin.

Lemma 3. Following from Lemma 1, suppose a radially unbounded Lyapunov function Wsatisfies Equation (14). If the parameters are chosen as expressed by Equation (20):

$$\mu_1 = \frac{1}{T_d \cdot \lambda \cdot \varrho\,(1-\beta_1)}, \quad \mu_2 = \frac{1}{T_d\,(1-\lambda)\,\varrho\,(\beta_2-1)}, \tag{20}$$

where $0 < \lambda < 1$ *and* $T_d > 0$denotes the predefined settling time, then the system exhibits a practical predefined-time stability. Consequently, for all $t \geq T_d$, the state z ultimately converges to the residual set $\boldsymbol{\Omega}$ defined in Equation (16).

3.2. Proposed VE-PdT-SMC Design.

The proposed controller was built on an integral VE-based sliding surface, defined by Equation (21):

$$\boldsymbol{\Sigma} = \boldsymbol{\varepsilon} + \int \left(k_1 ||\boldsymbol{\varepsilon}||^{2\lambda_1 \tanh(||\boldsymbol{\varepsilon}||^2)} \tanh\left(\frac{\boldsymbol{\varepsilon}}{\mu_1}\right) + k_2 \lfloor \boldsymbol{\varepsilon} \rceil^{\lambda_2} \right) dt, \tag{21}$$

where $k_1 = \dfrac{\sqrt{2}}{T_p\,\ell_1\,\upsilon_0} \exp^{\lambda_1/\exp}$, $\upsilon_0 \in (0,1)$, $\lambda_1 > 0$, $\ell_1 \in (0,1)$, $\lambda_0 = \dfrac{\lambda_2+1}{2}$, $\lambda_2 > 1$, $\mu_1 > 0$, $T_p > 0$ is the predefined settling time, and the operator $\lfloor \boldsymbol{\varepsilon}^{\beta} \rceil = [\lfloor \varepsilon_1 \rceil^{\beta} \operatorname{sgn}(\varepsilon_1), \lfloor \varepsilon_2 \rceil^{\beta} \operatorname{sgn}(\varepsilon_2), \textit{and } |\varepsilon_3|^{\beta} \operatorname{sgn}(\varepsilon_3)]^T \in \mathbb{R}^3$ Differentiating Equation (21) and substituting Equation (11) results in Equation (22):

$$\begin{aligned} \dot{\boldsymbol{\Sigma}} &= \dot{\boldsymbol{\varepsilon}} + k_1 \parallel \varepsilon \parallel^{2\lambda_1 \tanh(\|\boldsymbol{\varepsilon}\|^2)} \tanh\left(\frac{\boldsymbol{\varepsilon}}{\mu_1}\right) + k_2 \lfloor \varepsilon \rceil^{\lambda_2} \\ &= \left(\mathbf{A}\,\mathbf{i} - \mathbf{B}\,\mathbf{U} + \boldsymbol{\phi} + \boldsymbol{\Delta} - \dot{\mathbf{i}}_{\text{ref}}\right) + \boldsymbol{\Psi}, \end{aligned} \tag{22}$$

where $\boldsymbol{\Psi} = k_1 \|\boldsymbol{\varepsilon}\|^{2\lambda_1 \tanh(\|\boldsymbol{\varepsilon}\|^2)} \tanh\left(\frac{\boldsymbol{\varepsilon}}{\mu_1}\right) + k_2 \lfloor \boldsymbol{\varepsilon} \rceil^{\lambda_2} \in \mathbb{R}^3$ Using the inverse dynamics approach in Equation (22), the proposed robust VE-PdT-SMC law is expressed by Equation (23):

$$\begin{aligned} U = \mathbf{B}^{-1}\{&\mathbf{A}\,\mathbf{i} + \boldsymbol{\phi} - \dot{\mathbf{i}}_{\text{ref}} + \boldsymbol{\Psi} + \mathcal{K}_1 \parallel \Sigma \parallel^{2\beta_1 \tanh(\|\boldsymbol{\Sigma}\|^2)} \\ &\times \tanh\left(\frac{\boldsymbol{\Sigma}}{\mu_1}\right) + \mathcal{K}_2 \lfloor \boldsymbol{\Sigma} \rceil^{\beta_2} + c_1 \lfloor \boldsymbol{\Sigma} \rceil^{0}\} \end{aligned} \tag{23}$$

where $\mathcal{K}_1 = \frac{\sqrt{2}}{T_s\,\upsilon_0\,\ell_2} \exp^{\frac{\beta_1}{\exp}}$, $\mathcal{K}_2 = \frac{1}{2^{\beta_0} 3^{1-\beta_0} T_s (1-\ell_2)\,\upsilon_0\,(\lambda_0-1)}$, $\beta_0 = \frac{1+\beta_2}{2}$, $\mu_2 > 0, \ell_2 \in (0,1)$, $\beta_1 > 0$, $\beta_2 > 1$, and $c_1 \geq \overline{\Delta} > 0$. Here $\mathcal{K}_1$ and $\mathcal{K}_2$ are designed to ensure that the system converges within a predefined time. Meanwhile, the parameter c_1 ensures the system remains robust against model inaccuracies and external disturbances. This is achieved by utilizing the discontinuous sgn $(\boldsymbol{\Sigma})$ term to maintain stability. The next section presents a comprehensive stability analysis of the closed-loop system.

4. STABILITY ANALYSIS

Theorem 1. Given the HPS error model in Equation (11) and subject to Assumptions 1 and 2, the proposed robust VE-PdT-SMC strategy in Equation (23) ensures two-stage, predefined-time stability. First, the sliding surface reaches zero within a predefined time T_s. Following this, the tracking errors are forced to zero within the next predefined-time bound T_p. Consequently, the system states track the reference trajectories accurately, and the total convergence time is independent of the initial conditions.

Proof: The proof proceeds in two steps. First, the fact that $\boldsymbol{\Sigma}$ converges to zero in a predefined time is established. Next, the evidence that $\boldsymbol{\varepsilon}$ is predefined-time stable is provided, thereby deriving the required power from different energy sources as per the reference current trajectory.

Part 1: In this part, we show that the integral sliding variable $\boldsymbol{\Sigma}$ defined in Equation (21) is driven to zero in the predefined time T_s. To this end, we consider a Lyapunov function expressed by Equation (24):

$$V_1 = 1/2\boldsymbol{\Sigma}^T\boldsymbol{\Sigma}. \tag{24}$$

The time derivative of V_1 yields Equation (25):

$$\dot{V}_1 = \dot{\boldsymbol{\Sigma}}^T\boldsymbol{\Sigma}. \tag{25}$$

Substituting Equation (22) into Equation (25) gives Equation (26):

$$\dot{V}_1| = \boldsymbol{\Sigma}^T\left(\mathbf{A}\,\mathbf{i} - \mathbf{B}\,\mathbf{U} + \boldsymbol{\Delta} + \phi - \dot{\mathbf{i}}_{\text{ref}} + \boldsymbol{\Psi}\right) \tag{26}$$

Plugging the proposed robust VE-PdT control law from Equation (23) into Equation (26) yields Equation (27):

$$\begin{aligned} \dot{V}_1| &= \boldsymbol{\Sigma}^T\{-\mathcal{K}_1 \parallel \Sigma \parallel^{2\beta_1 \tanh(\|\boldsymbol{\Sigma}\|^2)} \tanh\left(\frac{\boldsymbol{\Sigma}}{\mu_1}\right) \\ &\quad - \mathcal{K}_2 \lfloor \boldsymbol{\Sigma} \rceil^{\beta_2} - c_1 \lfloor \boldsymbol{\Sigma} \rceil^{0} + \Delta\}, \\ &= -\mathcal{K}_1 \parallel \Sigma \parallel^{2\beta_1 \tanh(\|\boldsymbol{\Sigma}\|^2)} \boldsymbol{\Sigma}^T \tanh\left(\frac{\boldsymbol{\Sigma}}{\mu_1}\right) \\ &\quad - \mathcal{K}_2 \boldsymbol{\Sigma}^T |\Sigma|^{\beta_2} - c_1 \boldsymbol{\Sigma}^T |\Sigma|^{0} + \boldsymbol{\Sigma}^T\Delta, \\ &\leq -\mathcal{K}_1 \parallel \Sigma \parallel^{2\beta_1 \tanh(\|\boldsymbol{\Sigma}\|^2)} \boldsymbol{\Sigma}^T \tanh\left(\frac{\boldsymbol{\Sigma}}{\mu_1}\right) \\ &\quad - \mathcal{K}_2 \parallel \Sigma \parallel^{\beta_2+1} - c_1 \parallel \Sigma \parallel + \parallel \boldsymbol{\Sigma}^T \parallel \parallel \Delta \parallel \\ &= -\mathcal{K}_1 \parallel \Sigma \parallel^{2\beta_1 \tanh(\|\boldsymbol{\Sigma}\|^2)} \boldsymbol{\Sigma}^T \tanh\left(\frac{\boldsymbol{\Sigma}}{\mu_1}\right) \\ &\quad - \mathcal{K}_2 \parallel \Sigma \parallel^{\beta_2+1} . \\ &\quad - \underbrace{\left(c_1 - \bar{\Delta}\right)}_{:=\ \overline{k_d} \ > 0} \parallel \Sigma \parallel \end{aligned} \tag{27}$$

Because $\tanh\left(\parallel \boldsymbol{\Sigma} \parallel^2\right) \leq \parallel \boldsymbol{\Sigma} \parallel^2$, Equation (28) is obtained:

$$\begin{aligned} \min\left(\parallel \boldsymbol{\Sigma} \parallel^{2\beta_1 \tanh(\|\boldsymbol{\Sigma}\|^2)}\right) &\geq \min\left(\parallel \boldsymbol{\Sigma} \parallel^{2\beta_1 \|\boldsymbol{\Sigma}\|^2}\right) \\ &= \exp^{-\beta_1/\exp}. \end{aligned} \tag{28}$$

Moreover, using the inequality given in[34] for $\theta \in \mathbb{R}$, Equation (29) is obtained:

$$|\theta| - \theta \tanh(\theta/\epsilon) \leq \eta\epsilon, \tag{29}$$

where $\eta = 0.2785$, and $\epsilon > 0$. Consequently, Equation (30) is obtained[30]:

$$-\mathcal{K}_1 \mathbf{\Sigma}^T \tanh\left(\frac{\mathbf{\Sigma}}{\mu_1}\right) < -\mathcal{K}_1 \parallel \mathbf{\Sigma} \parallel + \mathcal{K}_1 n \mu_1 \eta, \tag{30}$$

where n is the number of elements in vector $\mathbf{\Sigma}$, i.e., 3.

Incorporating the relations in Equation (28) and Equation (30) into Equation (27), V'' can be expressed by Equation (31):

$$\begin{aligned}\dot{V}_1 &\leq -\mathcal{K}_1 \exp^{-\frac{\beta_1}{\exp}} \parallel \mathbf{\Sigma} \parallel - \mathcal{K}_2 \parallel \mathbf{\Sigma} \parallel^{\beta_2+1} - \overline{k_d} \parallel \mathbf{\Sigma} \parallel \\ &\quad + \mathcal{K}_1 n \mu_1 \eta \\ &\leq -\mathcal{K}_1 \exp^{-\frac{\beta_1}{\exp}} \parallel \mathbf{\Sigma} \parallel - \mathcal{K}_2 \parallel \mathbf{\Sigma} \parallel^{\beta_2+1} + \wp,\end{aligned} \tag{31}$$

where $\wp = \mathcal{K}_1 n \mu_1 \eta$. After substituting the values of $\mathcal{K}_1$ and $\mathcal{K}_2$, Equation (32) is obtained:

$$\dot{V}_1 \leq -\frac{2}{T_s\, \upsilon_0\, \ell_2} V_1^{1/2} - \frac{1}{T_s\, (\ell_2 - 1)\ \upsilon_0\ (\beta_0 - 1)} V_1^{\beta_0} + \bar{\wp}, \tag{32}$$

where $\bar{\wp} = \mathcal{K}_1 n \exp^{-\frac{\beta_1}{\exp}} \mu_1 \eta$. By applying Lemma 3, the inequality presented in Equation (32) confirms that the sliding surface converges to zero within a predefined duration. This completes the first part of the stability analysis, demonstrating that the sliding mode is achieved regardless of the system's initial state.

Part 2: Having established convergence of $\mathbf{\Sigma}$ in Part 1, we now show that once the system reaches the sliding manifold, the tracking error (ε) itself converges to zero in the predefined time (T_p). As the system enters the sliding phase, both the sliding surface and its rate of change go to zero, i.e., the conditions $\mathbf{\Sigma} = \mathbf{0}$ and $\dot{\mathbf{\Sigma}} = \mathbf{0}$ are maintained. Consequently, Equation (22) can be reformulated as Equation (33):

$$\begin{aligned}\dot{\mathbf{\Sigma}} &= \dot{\boldsymbol{\varepsilon}} + k_1 \parallel \boldsymbol{\varepsilon} \parallel^{2\lambda_1 \tanh(\|\boldsymbol{\varepsilon}\|^2)} \tanh\left(\frac{\varepsilon}{\mu_1}\right) \\ &\quad + k_2 \lfloor \boldsymbol{\varepsilon} \rceil^{\lambda_2} = 0 \\ \text{or } \dot{\boldsymbol{\varepsilon}} &= -k_1 \parallel \boldsymbol{\varepsilon} \parallel^{2\lambda_1 \tanh(\|\boldsymbol{\varepsilon}\|^2)} \tanh\left(\frac{\varepsilon}{\mu_1}\right) - k_2 \lfloor \boldsymbol{\varepsilon} \rceil^{\lambda_2}\end{aligned} \tag{33}$$

To verify the predefined-time convergence properties of $\boldsymbol{\varepsilon}$, we introduce a second Lyapunov function (V_2) as expressed by Equation (34):

$$V_2 = \frac{1}{2} \boldsymbol{\varepsilon}^T \boldsymbol{\varepsilon} \tag{34}$$

By differentiating V_2 with respect to time and incorporating the error dynamics from Equation (33), we obtain Equation (35):

$$\begin{aligned}\dot{V}_2 &= \boldsymbol{\varepsilon}^T \dot{\boldsymbol{\varepsilon}} \\ &= \boldsymbol{\varepsilon}^T \left(-k_1 \parallel \boldsymbol{\varepsilon} \parallel^{2\lambda_1 \tanh(\|\boldsymbol{\varepsilon}\|^2)} \tanh\left(\frac{\boldsymbol{\varepsilon}}{\mu_1}\right) - k_2 \lfloor \boldsymbol{\varepsilon} \rceil^{\lambda_2}\right)\end{aligned} \tag{35}$$

By following a similar approach to that in the first part, we can obtain Equation (36):

$$\dot{V}_2 \leq -\frac{2}{T_p\, \ell_1\, \upsilon_0} \mu_1 V_2^{\frac{1}{2}} - \frac{1}{T_p\, (\ell_1 - 1)\ \upsilon_0\ (\lambda_0 - 1)} V_2^{\lambda_0} + \varpi \tag{36}$$

where $\varpi = k_1 n \exp^{-\frac{\lambda_1}{\exp}} \mu_1 \eta > 0$. Because the resulting inequality in Equation (36) meets the predefined-time stability condition in Lemma 3, the tracking error ($\boldsymbol{\varepsilon}$) is approximately zero within a set timeframe. This completes the overall stability of the closed-loop system.

Remark 1. With the error vector ($\boldsymbol{\varepsilon}$) converging to zero at a predefined time (T_p), Equation (8) guarantees that the DC-link voltage (υ_{dc}) also reaches its reference value $\upsilon_{dc,r}$within the same time bound.

Remark 2 (chattering attenuation). Conventional SMC methods commonly suffer from chattering caused by the discontinuous switching term sgn ($\mathbf{\Sigma}$), which excites high-frequency dynamics in the converter switches. In the proposed control law (23), three structural features jointly mitigate chattering. First, $\mathcal{K}_1 \parallel \mathbf{\Sigma} \parallel^{2\beta_1 \tanh(\|\mathbf{\Sigma}\|^2)}$ and $\mathcal{K}_2 |\mathbf{\Sigma}|^{\beta_2}$ are VE terms, which automatically reduce their magnitude as $\parallel \mathbf{\Sigma} \parallel$ approaches zero, so that the controller transitions from an aggressive far-from-equilibrium action to a soft near-equilibrium action without manual gain scheduling. Second, the smooth tanh $\left(\frac{\mathbf{\Sigma}}{\mu_1}\right)$ approximation replaces the discontinuous sign function over the dominant portion of the control action and confines the residual switching activity to a small boundary layer of width (μ_1). Third, the discontinuous term $c_1 |\mathbf{\Sigma}|^0$ is retained only with a minimal switching gain that satisfies $c_1 \geq \Delta$, which is sufficient to dominate the bounded uncertainty without injecting unnecessarily large discontinuous activity into the duty ratios. Consequently, the closed-loop control signals ($\mathbf{U}$) remain practically smooth across the simulated urban dynamometer driving schedule (UDDS) profile, as observed in the results presented in Section 5.

Remark 3 (sensitivity against measurement noise and parameter uncertainties). The robustness of the proposed VE-PdT-SMC against measurement noise and parameter uncertainties can be analyzed through the inequality in Equation (31). Bounded measurement noise on (i_{fc}, i_b, i_{uc}, and υ_{dc}) appears as an additional bounded perturbation that can be absorbed into the lumped uncertainty vector (Δ). Provided the switching gain is selected to dominate the worst-case combined bound, i.e., $c_1 \geq \Delta_{nom} + \Delta_{noise}$, the practical predefined-time stability established in Theorem 1 is preserved, and the trajectories converge to a residual set whose size scales linearly with the perturbation amplitude. Similarly, parametric mismatches in the converter elements (R_{fc}, R_b, R_{uc}, L_{fc}, L_b, L_{uc}, C_{dc}) appear as bounded multiplicative perturbations of matrices $\mathbf{A}$ and $\mathbf{B}$ in Equation (12) and are likewise absorbed by the lumped uncertainty term, provided Assumption 2 holds with an appropriately enlarged bound. The smooth VE action prevents these perturbations from being amplified into high-frequency control activity, whereas the explicit settling-time parameter T_s remains a guaranteed upper bound on the convergence time.

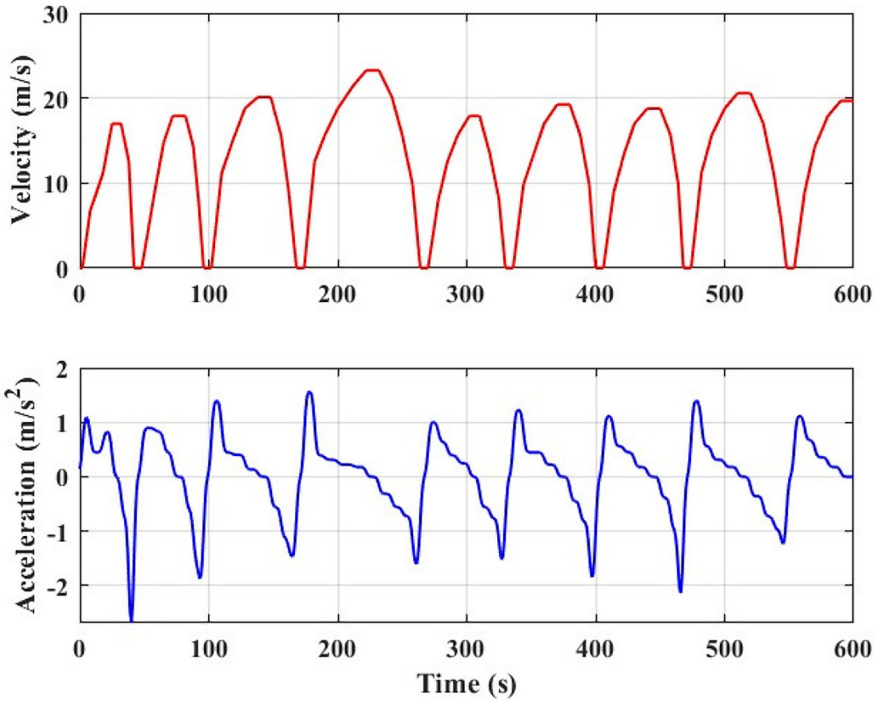

Figure 3. Velocity and acceleration profiles

5. RESULTS AND DISCUSSION

The performance of the proposed VE-PdT-SMC for the FCEV hybrid powertrain was evaluated via numerical analysis. The robustness of the proposed strategy was evaluated by introducing multiple source uncertainties simultaneously. These included fuel cell voltage drops from 350 to 320 V (an 8.6% decrease), UC voltage deviations of up to 12.5% beyond the nominal 200 V, and battery voltage fluctuations between 288 and 320 V. These variations were injected into the simulation at $t = 200$ s.

To represent realistic driving conditions, the load current (i_o) was calculated using the UDDS [35], a standardized USA Environmental Protection Agency profile for urban driving. The velocity and acceleration profiles under the UDDS are illustrated in Figure 3 for 600 s. The corresponding load current was derived from the longitudinal dynamics of the vehicle as expressed by Equation (37):

$$i_o = \frac{1}{0.75 \times 400}\left[0.5\, p_a v_t^2 A C_x + M_g C_r + M\frac{dv_t}{dt}\right] v_t, \quad (37)$$

where i_o is the load current, p_a denotes the air density, v_t is the vehicle speed, A is the frontal area, C_x is the aerodynamic drag coefficient, M_g represents the gradient resistance, C_r is the rolling resistance coefficient, M is the vehicle mass, and dv_t/dt is the vehicle acceleration. The system and control parameters used in the simulations are summarized in Tables 2 and 3, respectively.

Figure 4 presents the simulation results when the fuel cell voltage (v_{fc}) undergoes a step decrease from 350 V to 320 V (8.6% drop) at $t = 400$ s, followed by a second disturbance at $t \approx 550$ s. As shown in Figure 4(a), the DC-link voltage v_{dc} is maintained close to the reference value of 400 V throughout the entire simulation under the dynamic load demand of the UDDS drive cycle. A transient overshoot of approximately 5 V (1.25%) is observed at the instant of the uncertainty injection, after which the proposed controller rapidly drives v_{dc} back to its reference value. The fuel cell current (i_{fc}) also follows the dynamic load profile. Thus, the proposed controller simultaneously regulates the DC-link voltage and tracks the source currents under the most severe uncertainty scenario. The tracking error response, illustrated in Figure 4(b), also confirms this behavior. The DC voltage error ($e_{v_{dc}}$) exhibits a small transient deviation of approximately −6 V at the disturbance instant, which is rapidly suppressed to near zero by the VE-PdT-SMC within a predefined time. The fuel cell

Table 2. *Parameter values of the hybrid power system*

Parameter	Value	Parameter	Value	Parameter	Value
L_1	3.3 mH	L_2	3.3 mH	L_3	3.3 mH
R_1	0.002 Ω	R_2	0.002 Ω	R_3	0.002 Ω
C	0.66 mF	v_{fc}	350 V	v_{bat}	288 V
v_{uc}	205 V	V_{dc}^*	400 V	σ	1.05
p_a	1.225 kg/m^3	C_x	0.19	M_g	1066 N
C_r	0.0048	A	1.8 m^2	M	500 kg

Table 3. *Proposed VE-PdT-SMC parameter values*

Parameter	Value	Parameter	Value	Parameter	Value
		Sliding surface parameters			
T_x	0.5 s	ℓ_1	0.9	μ_1	1.5
λ_1	0.12	λ_2	1.7	v_0	0.99
		Controller parameters			
T_s	0.02 s	ℓ_2	0.5	μ_2	0.5
β_1	0.1	β_2	1.7	c_1	1.05

current error ($e_{i_{fc}}$) also converges to zero quickly following the disturbance.

Figure 5 shows the controller performance when the battery voltage (v_{bat}) increases from 288 to 320 V (+11.2%) at $t = 600$ s. As evident from Figure 5(a), the DC-link voltage (v_{dc}) remains tightly regulated at the 400 V reference despite this variation. The transient deviation is small, with a peak overshoot of approximately 0.1 V (0.025%), which is significantly lower than that observed under the fuel cell voltage uncertainty. This demonstrates that the bidirectional converter interfacing the battery is effectively controlled by the proposed scheme. Meanwhile, i_{fc} continues to accurately track the UDDS-driven load demand, confirming seamless multi-source coordination. The tracking errors in Figure 5(b) further confirm the efficient performance under battery voltage fluctuations. The DC voltage error ($e_{v_{\text{dc}}}$) is confined within a negligibly small band of ±0.1 V, whereas the

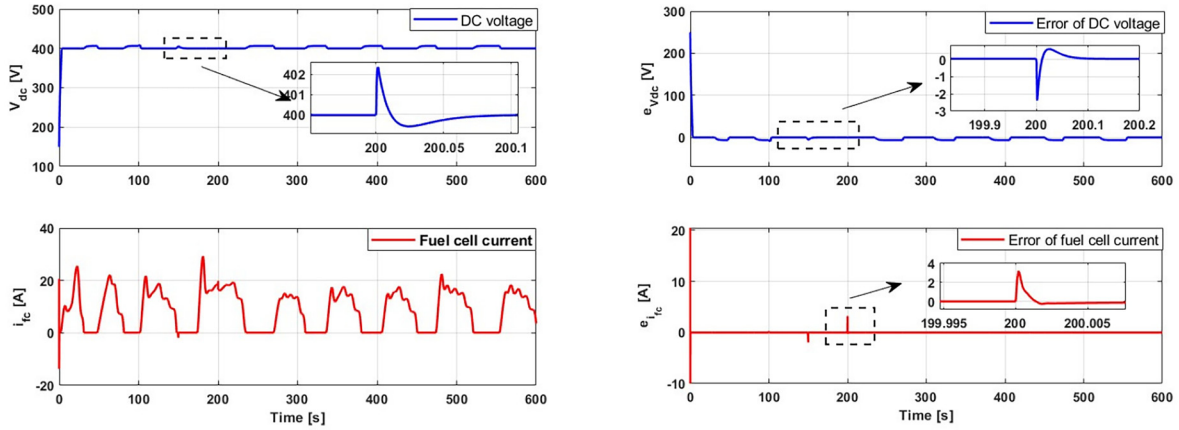

Figure 4. Simulation results under fuel cell voltage uncertainty (v_{fc}: 350 V → 320 V, −8.6%). (a) v_{dc} and i_{fc} under a change in v_{fc}. (b) Tracking errors of v_{dc} and i_{fc} during the change in v_{fc}

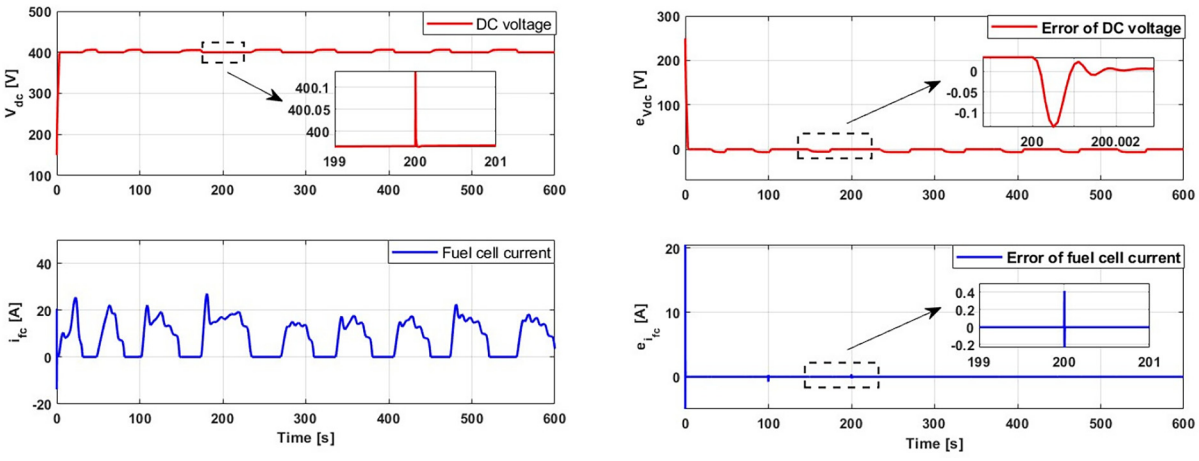

Figure 5. Simulation results under battery voltage uncertainty (v_{bat}: 288 V → 320 V, +11.2%). (a) v_{dc} and i_{fc} under a change in v_{bat}. (b) Tracking errors of v_{dc} and i_{fc} during the change in v_{bat}

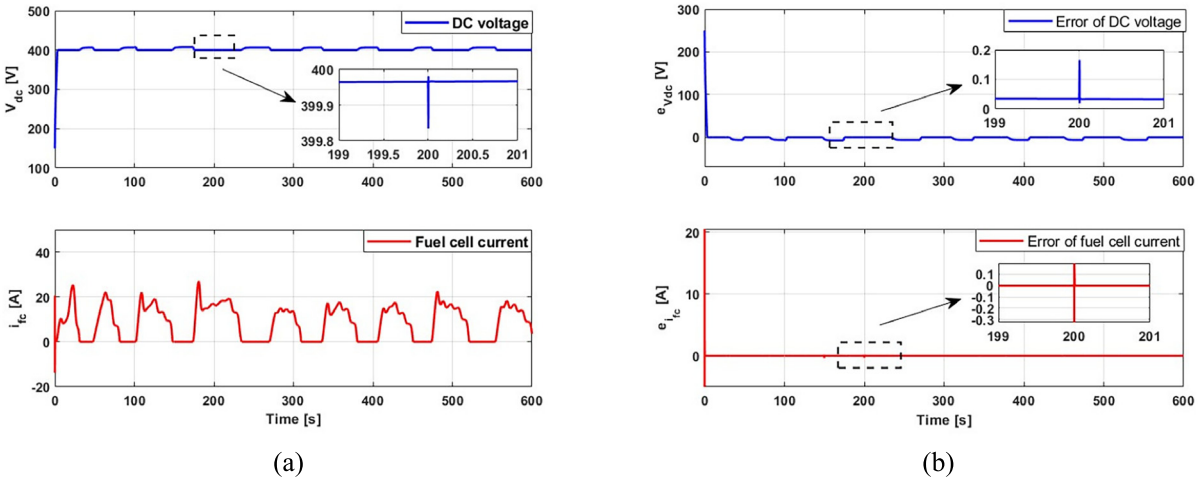

Figure 6. Simulation results under ultracapacitor voltage uncertainty (v_{uc}: 200 V → 225 V, +12.5%). (a) v_{dc} and i_{fc} under a change in v_{uc}. (b) Tracking errors of v_{dc} and i_{fc} during the change in v_{uc}

fuel cell current error ($e_{i_{fc}}$) converges to zero within milliseconds of the disturbance injection.

Figure 6 presents the results when the UC voltage (v_{uc}) increases from 200 to 225 V (+12.5%) at $t = 800$ s. As shown in Figure 6(a), the DC-link voltage (v_{dc}) exhibits the smallest transient deviation among all three uncertainty scenarios, with a dip of approximately 0.1 V during fluctuation. The controller immediately restores the voltage to 400 V, demonstrating a fast, robust response to UC voltage variations. The fuel cell current (i_{fc}) continues to track the load profile with high fidelity throughout this scenario. The error profiles in Figure 6(b) show that both $e_{v_{dc}}$ and $e_{i_{fc}}$ are driven to zero almost instantaneously following the disturbance. The peak DC voltage error remains below 0.2 V, and the fuel cell current error stays within ±0.3 A during the transient. These results, combined with the previous two cases, demonstrate that the proposed VE-PdT-SMC delivers consistent, robust performance across all source-uncertainty scenarios.

To provide quantitative benchmarking as required to assess the claimed performance improvements, a finite time SMC (FTSMC) [21] was implemented on the same triple-source FCEV model under identical reference trajectories, uncertainty injections, and UDDS load demand. FTSMC uses the same sliding surface structure but replaces the variable-exponent predefined-time gains with fixed gains tuned to yield the smallest possible steady-state error. The following performance indices are evaluated for each current-tracking channel over the full 600 s simulation: root-mean-square error (RMSE), integral absolute error (IAE), integral squared error (ISE), integral time-weighted absolute error (ITAE), and peak absolute error (Max |e|). The results are summarized in Table 4.

As evident from Table 4, the proposed method achieves RMSE reductions of 83–95% across all three current channels relative to the FTSMC benchmark. The IAE is reduced by 97.8–99.8%, confirming that the proposed controller accumulates a substantially lower tracking error over the entire drive cycle. ITAE improvements exceeding 99% for the fuel cell and battery current channels indicate that any residual transient error is rapidly suppressed, consistent with the predefined-time convergence guarantee established in Theorem 1. The peak absolute error is reduced by approximately 70% or more in all channels, demonstrating superior robustness against the simultaneous source-side voltage uncertainties injected at $t = 200$ s. These results collectively confirm that replacing the fixed-gain switching structure of the FTSMC with the VE FxT mechanism yields a quantifiable and substantial improvement in both transient and steady-state performance, validating the contributions claimed in Section 1.

The results from all case studies confirm the validity of the proposed control framework and demonstrate its capability to achieve the desired performance objectives in the presence of source uncertainties. While the study is limited to the numerical analysis, the findings provide strong evidence of the robustness and practical applicability of the proposed VE-PdT-SMC.

Table 4. *Quantitative error metrics*

		Error			
Controller	**Scenario**	**RMSE**	**IAE**	**ISE**	**ITAE**
	v_{bat} change	0.3100	0.5045	3.670	1.1047
FTSMC[21]	v_{fc} change	0.3103	0.6060	1.749	3.125
	v_{sc} change	0.3100	0.4963	2.669	1.1036
	v_{bat} change	0.0159	0.0171	0.1468	0.2549
Proposed	v_{fc} change	0.0162	0.0230	0.1517	1.3343
	v_{sc} change	0.0159	0.0168	0.1467	0.2218

6. CONCLUSIONS

In this study, we developed a robust control framework based on a VE PdT strategy to manage the multiple energy dynamics of an FCEV hybrid powertrain under voltage fluctuations. The primary objective was to maintain a steady 400 V DC-link voltage while efficiently meeting load demands through coordinated use of multiple energy sources. A key advantage of the proposed VE-PdT-SMC scheme over traditional methods is its ability to ensure that tracking errors converge to zero within a strictly predefined timeframe. This characteristic provides a more reliable performance and simplifies the tuning process for practical, real-world applications. Mathematically, we proved this through a rigorous Lyapunov stability analysis, which demonstrated that the system was PdT stable, regardless of the initial operating conditions. Finally, extensive numerical evaluations under various uncertainty scenarios were conducted to confirm that the proposed strategy effectively balanced energy distribution. These results highlight a substantial improvement in transient response and overall operational efficiency for fuel cell vehicles during realistic driving cycles. Overall, the study findings demonstrate that the proposed control scheme is suitable for practical FCEV applications. However, despite these advantages, the approach assumes bounded uncertainties and has been validated only through simulations, with possible computational challenges for real-time implementation. In addition, some residual chattering may occur under high measurement noise. The scope for future work is to focus on experimental and hardware-in-the-loop validation, development of fault-tolerant and adaptive extensions, and integration with higher-level energy management strategies for practical FCEV applications.

AFFILIATIONS AND AUTHOR DETAILS

Undergraduate Author

Maryam Abdulaziz Alsalman – *Control & Instrumentation Engineering Department, King Fahd University of Petroleum & Minerals, Dhahran 31261, Saudi Arabia*; 0009-0001-3434-3461
Email: s202246360@kfupm.edu.sa ;

Corresponding Author

Syed Muhammad Amrr – *Research Mentor, Assistant Professor, Control & Instrumentation Engineering Department, King Fahd University of Petroleum & Minerals, Dhahran 31261, Saudi Arabia*; 0000-0001-5084-5472
Email: syed.amrr@kfupm.edu.sa

ACKNOWLEDGEMENTS

The authors would like to acknowledge the support provided by the Control & Instrumentation Engineering Department and the Interdisciplinary Research Center for Sustainable Energy System at King Fahd University of Petroleum & Minerals. The authors also extend their appreciation to Mr. Abdullah Abushokor, a Ph.D. student at CIE Department, KFUPM, for his valuable assistance in numerical analysis, technical discussions, and valuable suggestions that contributed to the development of this work.

REFERENCES

(1) Shemami, M. S., Amrr, S. M., Alam, M. S. & Asghar, M. J. Reliable and economy modes of operation for electric vehicle-to-home (V2H) system. In *Proc. 5th IEEE Uttar Pradesh Section Int. Conf. Electrical, Electronics & Computer Eng. (UPCON)*, 1–6 (2018).

(2) Zaery, M., Wang, P., Wang, W. & Xu, D. A novel optimal power allocation control system with high convergence rate for DC microgrids cluster. *Energies* **15**, 3994 (2022).

(3) Chan, C. C., Bouscayrol, A. & Chen, K. Electric, hybrid, and fuel-cell vehicles: Architectures and modeling. *IEEE Trans. Veh. Technol.* **59**, 589–598 (2009).

(4) Ali, H., Zaery, M., Amrr, S. M., Hussain, S. S., Vital, V. & Abido, M. A. Enhanced voltage stability for DC microgrids integrating hybrid electric vehicles with virtual inertia and damping control. *Transp. Res. Procedia* **84**, 571–578 (2025).

(5) Förster, R., Kaiser, M. & Wenninger, S. Future vehicle energy supply—sustainable design and operation of hybrid hydrogen and electric microgrids. *Appl. Energy* **334**, 120653 (2023).

(6) Samiullah, M., Amrr, S. M. & Al-Awami, A. T. Adaptive integral SMC for power conversion of PEM fuel cell with practical fixed time stability. In *Proc. 59th IEEE Industry Applications Society Annual Meeting (IAS)*, 1–6 (2024).

(7) Alzyod, M. N., Al-Awami, A. T., Jeong, Y. & Kim, S. A multi-phase energy management system for hybrid fuel cell drones. In *Proc. IEEE Transp. Electrif. Conf. and Expo (ITEC)*, 1–6 (2024).

(8) Bidyadhar, R. S. P. Double integral sliding mode MPPT control of a photovoltaic system. *IEEE Trans. Control Syst. Technol.* **24**, 285–292 (2016).

(9) Alireza, J. K. S. A supervisory energy management control strategy in a battery/ultracapacitor hybrid energy storage system. *IEEE Trans. Transp. Electrif.* **1**, 223–231 (2015).

(10) Carignano, M., Roda, V., Costa-Castelló, R., Valiño, L., Lozano, A. & Barreras, F. Assessment of energy management in a fuel cell/battery hybrid vehicle. *IEEE Access* **7**, 16110–16122 (2019).

(11) Khaligh, A. & Li, Z. Battery, ultracapacitor, fuel cell, and hybrid energy storage systems for electric, hybrid electric, fuel cell, and plug-in hybrid electric vehicles: State of the art. *IEEE Trans. Veh. Technol.* **59**, 2806–2814 (2010).

(12) Rahman, A. U., Ahmad, I. & Malik, A. S. Variable structure-based control of fuel cell-supercapacitor-battery based hybrid electric vehicle. *J. Energy Storage* **29**, 101365 (2020).

(13) Essoufi, M., Hajji, B. & Rabhi, A. Fuzzy logic based energy management strategy for fuel cell hybrid electric vehicle. In *Proc. International Conference on Electrical and Information Technologies (ICEIT)*, 1–7 (2020).

(14) Mazouzi, A., Hadroug, N., Alayed, W., Hafaifa, A., Iratni, A. & Kouzou, A. Comprehensive optimization of fuzzy logic-based energy management system for fuel-cell hybrid electric vehicle using genetic algorithm. *Int. J. Hydrogen Energy* **81**, 889–905 (2024).

(15) Rodriguez, R., Trovão, J. P. F. & Solano, J. Fuzzy logic-model predictive control energy management strategy for a dual-mode locomotive. *Energy Convers. Manag.* **253**, 115111 (2022).

(16) Song, K., Huang, X., Xu, H., Sun, H., Chen, Y. & Huang, D. Model predictive control energy management strategy integrating long short-term memory and dynamic programming for fuel cell vehicles. *Int. J. Hydrogen Energy* **56**, 1235–1248 (2024).

(17) Kraa, O. *et al.* Energy management of fuel cell/supercapacitor hybrid source based on linear and sliding mode control. *Energy Procedia* **74**, 1258–1264 (2015).

(18) Ahmed, M., Masood, U., Azeem, M. K., Ahmad, I. & Jabbar, A. U. Barrier function based adaptive sliding mode controller for the hybrid energy storage system of plug-in hybrid electric vehicles. *J. Energy Storage* **72**, 108051 (2023).

(19) Samiullah, M., Al-Awami, A. T., Amrr, S. M., Zaery, M. & Abido, M. A. Advanced sliding mode control for battery-backed hybrid power system in a fuel cell electric vehicle with a fixed-time convergence. *Energy Convers. Manag.: X* **27**, 101174 (2025).

(20) Amrr, S. M., Ahmad, J., Waheed, S. A., Sarwar, A., Saidi, A. S. & Nabi, M. Finite-time adaptive sliding mode control of a power converter under multiple uncertainties. *Front. Energy Res.* **10**, 901606 (2022).

(21) Fadil, H. E., Idrissi, Z. E., Intidam, A., Rachid, A., Koundi, M. & Bouanou, T. Nonlinear control and energy management of the hybrid fuel cell and battery power system. *Int. J. Model. Identif. Control* **36**, 89–103 (2020).

(22) Masood, U., Azeem, M. K., Ahmad, I. & Jabbar, A. ul. Robust adaptive nonlinear control of plug-in hybrid electric vehicles for vehicle-to-grid and grid-to-vehicle power flow with hybrid energy storage system. *ISA Trans.* **139**, 406–424 (2023).

(23) Samiullah, M., Amrr, S. M., Al-Awami, A. T., AbouOmar, M. S. & El Ferik, S. Robust high gain control for uncertain hybrid powertrain systems in fuel cell electric vehicles. *Transp. Res. Procedia* **84**, 400–407 (2025).

(24) AlKawak, O. A., Kumar, J. R. R., Daniel, S. S. & Reddy, C. V. K. Hybrid method based energy management of electric vehicles using battery-super capacitor energy storage. *J. Energy Storage* **77**, 109835 (2024).

(25) Moulay, E., Léchappé, V., Bernuau, E. & Plestan, F. Robust fixed-time stability: Application to sliding-mode control. *IEEE Trans. Autom. Control* **67**, 1061–1066 (2021).

(26) Liu, X., Jia, C. & Wang, H. Practical variable exponent fixed-time nonsingular sliding mode control for nonlinear systems and its applications. *IEEE Trans. Autom. Sci. Eng.* **22**, 10871–10880 (2025).

(27) Nath, K., Patel, N., Kar, I. N. & Sivaramakrishnan, J. Design of fixed-time sliding mode control using variable exponents. *IFAC J. Syst. Control* **30**, 100287 (2024).

(28) Abushokor, A. & Amrr, S. M. Variable exponent fixed-time optimized sliding mode for quadrotor attitude control. In *Proc. 60th IEEE Industry Applications Society Annual Meeting (IAS)*, 1–6 (2025).

(29) Zhang, H., Wu, X. & Xiao, B. Variable-exponent sliding mode control of input-constrained systems: Application to spacecraft attitude regulation. *IEEE Trans. Aerosp. Electron. Syst.* **62**, 10609–10619 (2026).

(30) Li, Y., Sahoo, S., Dragičević, T., Zhang, Y. & Blaabjerg, F. Stability-oriented design of model predictive control for DC/DC boost converter. *IEEE Trans. Ind. Electron.* **71**, 922–932 (2023).

(31) Hossain, M. I., Hamanah, W. M., Mamdouh, M., Al-Awami, A. T. & Abido, M. Bidirectional power flow control of grid-to-battery and battery-to-grid systems for energy storage application of microgrids. In *Proc. Saudi Arabia Smart Grid (SASG)*, 1–6 (2022).

(32) Zhang, H., Li, B., Xiao, B., Yang, Y. & Ling, J. Nonsingular recursive-structure sliding mode control for high-order nonlinear systems and an application in a wheeled mobile robot. *ISA Trans.* **130**, 553–564 (2022).

(33) Wang, G., Zuo, Z. & Wang, C. Robust consensus control of second-order uncertain multiagent systems with velocity and input constraints. *Automatica* **157**, 111226 (2023).

(34) U.S. Environmental Protection Agency. Dynamometer drive schedules (2024); https://www.epa.gov/vehicle-and-fuel-emissions-testing/dynamometer-drive-schedules.